Highly stable coherent nanoprecipitates via diffusion-dominated solute uptake and interstitial ordering

Hang Xue, Chong Yang, Frédéric De Geuser, Peng Zhang, Jinyu Zhang, Bin Chen, Fuzhu Liu, Yong Peng, Jianjun Bian, Gang Liu, et al.

Highly stable coherent nanoprecipitates via interstitially ordered diffusion-dominated solute uptake

Hang Xue[1,+], Chong Yang[1,+], Frederic De Geuser[2,+], Peng Zhang[1], Jinyu Zhang[1], Bin Chen[3], Fuzhu Liu[1], Yong Peng[3], Jianjun Bian[4], Gang Liu[1,*], Alexis Deschamps[2,*], Jun Sun[1,*]

1. State Key Laboratory for Mechanical Behavior of Materials, Xi'an Jiaotong University, Xi'an 710049, China

2. CNRS, Grenoble INP, SIMaP, Université Grenoble Alpes, Grenoble 38000, France

3. School of Materials and Energy and Electron Microscopy Centre of Lanzhou University, Lanzhou University, Lanzhou 730000, China

4. Department of Industrial Engineering, University of Padova, Via Gradenigo 6/a, Padua, 35131, Italy

Abstract — Lightweight design strategies and advanced energy applications call for high-strength Al alloys that can serve at 300 – 400 °C temperature range. However, the present commercial high-strength Al alloys are limited to low-temperature applications < ~150 °C, because the antagonism between high thermal stability (preferentially associated with slow-diffusing solutes) and large volume fraction (mostly derived from high-solubility and fast-diffusing solutes) innate to coherent nanoprecipitates remains unsolved. Here we demonstrate an interstitial solute stabilizing strategy to produce highly-stable coherent nanoprecipitates (termed V phase) in Sc-added Al-Cu-Mg-Ag alloys that have a strong coarsening-resistance up to ~ 400 ºC and simultaneously a volume fraction of ~ 1.8 vol.%. The assembling of slow-diffusing Sc and fast-diffusing Cu atoms into coherent V is triggered by a coherent ledge-aided in-situ phase transformation from early-formed Cu-rich Ω nanoprecipitates, with diffusion-dominated Sc uptake and self-organization into interstitially ordering. Stable V nanoprecipitates, with an inherited high density, enable the Al alloys to reach an unprecedent creep resistance as well as exceptional tensile strength (~ 100 MPa) at 400 ºC. We envisage that the ledge-mediated interaction between slow- and fast-diffusing atoms may pave the way for the stabilization of coherent nanoprecipitates toward advanced 400 ºC-level light alloys, which could be readily adapted to large-scale industrial production.

+: These authors contribute equally to the paper.

* Corresponding authors: lgsammer@xjtu.edu.cn (GL), alexis.deschamps@grenoble-inp.fr (AD), junsun@xjtu.edu.cn (JS)

Main

Since the first discovery of age-hardening behavior in duralumin over one hundred years ago, alloys strengthened by nanoprecipitates have been applied extensively in industrial fields[1-4]. Aluminum (Al) alloys, deriving their high strength from nanoprecipitates, are the primary materials of choice for lightweight engineering[5]. However, commercial high-strength Al alloys are still limited to low-temperature applications < ~150 °C [6-8], far from matching a critical requirement of 300-400 °C service by modern industrial development[9,10], and the thermal stability achieved by alloys under development is limited to 300-350 °C. Such a long-standing temperature bottleneck ailing Al alloys is mainly related to the nanoprecipitates that either suffer from severe coarsening (Ostwald ripening) at elevated temperatures which may additionally involve undesirable phase transformation into coarse equilibrium phase [11,12] or lack a sufficiently high volume fraction to ensure sufficient strengthening response[13,14]. A high thermal stability and a large volume fraction are both necessarily required for heat-resistant nanoprecipitates[15], but they are mutually exclusive in Al alloys. Normally, high-solubility and fast-diffusing solutes (such as Cu, Zn, and Si) added in the Al alloys do constitute nanoprecipitates with a large volume fraction (> ~1.0 vol.%) but with insufficient thermal stability[16,17]. On the contrary, slow-diffusing solutes (such as Sc, Ti, and Zr) can lead to nanoprecipitates with high stability[18,19] but in inadequate volume fraction (< 0.3 vol.%). As there is a discrepancy of several orders of magnitude in diffusivity between the two sets of solutes[20], it is a challenge to assemble the high-solubility and slow-diffusing solutes into high-stability and high-fraction coherent nanoprecipitates for the design of creep-resistant Al alloys (see Supplementary Fig. 1).

In literature reports, interfacial solute segregation has proved [21,22] to be an effective approach that couples the two solutes at nanoprecipitate/matrix interfaces in Al-Cu-based alloys. Slow-diffusing solutes (*e.g.*, Sc[21] or Mn/Zr[22]) segregated at the interfaces stabilize the nanoprecipitates by reducing the interfacial energy and blocking the trans-interface diffusion[23], and

the high-solubility solute (*i.e.*, Cu) develop θ'-Al_2Cu nanoprecipitates with a large volume fraction that provides sufficient strengthening. However, interfacial solute segregation works invalidly at high temperatures > 350 ºC, as the interfacial solute segregation layer no longer remains intact [24,25]. Alternatively, in-situ phase transformation is a potential way to overcome this dilemma: high-content nanoprecipitates based on high-solubility and fast-diffusing solutes are expected to be first produced at relatively low aging temperature, and an in-situ phase transformation to be subsequently stimulated at higher temperature by combining slow-diffusing solutes toward a high stability. Nevertheless, no active mechanism has been yet reported that would trigger such an in-situ phase transformation within coherent nanoprecipitates, involving a quick entrance and periodical occupancy of foreign, slow diffusing solutes. Here in this work, we show that slow-diffusing Sc and high-solubility Cu solutes blend periodically into a highly stable coherent (Al,Cu,Sc)-based nanoprecipitate (termed V phase) in an Al-Cu-Mg-Ag alloy microalloyed with Sc. Although Sc has a diffusivity two orders of magnitude smaller than that of Cu[21], these two species can be alternately ordered within the V phase through a complex dual-step precipitation mechanism. By using various complementary experimental approaches working at different scales, we demonstrate an in-situ phase transformation at elevated temperature of prior Cu-rich Ω nanoprecipitates into the (Cu, Sc)-rich V phase. This template-directed phase transformation occurs via diffusion-dominated Sc uptake and interstitial occupancy, driven by an unexpected coherent ledge-aiding mechanism. The V nanoprecipitates, with a large number density inherited from their Ω precursors and an enhanced thermal stability brought by the interstitial Sc sublattice, result in an extreme creep-resistance at 400 ºC.

High thermal stability and outstanding creep-resistance

We used a cast Al-4.5Cu-0.3Mg-0.4Ag (wt.%) alloy (hereafter denoted as Al-Cu-Mg-Ag alloy) as the base material (see Methods). For comparison, an Al-4.5Cu (wt.%) model alloy that is well known to be strengthened by $\{100\}_\alpha$-oriented θ'-Al_2Cu nanoprecipitates was also studied.

After ageing at 185 °C, the microstructure of the Al-Cu-Mg-Ag alloy is characterized by plate-like Ω nanoprecipitates oriented along $\{111\}_\alpha$ habit planes (Fig. 1a), with an average radius of ~ 20 nm, a number density of ~ 4.4×10^{21} m^{-3}, and a volume fraction of ~2.5 vol.% (see statistical results in Supplementary Fig. 2). The Ω nanoprecipitates, constituted by high-solubility Cu and segregated by Mg and Ag at the interfaces, are well known to retain coherency up to ~ 200 ºC[26,27]. At higher temperature, they undergo rapid coarsening and finally transform into equilibrium θ-Al_2Cu at > ~ 300 ºC[28]. Such a thermal instability was evidenced in the present Al-Cu-Mg-Ag alloy when aged at 400 ºC. Only after 15 min ageing, the Ω nanoprecipitates quickly coarsened to a large size (average radius of ~ 260 nm and thickness of ~ 25 nm) and a significantly reduced density of ~ 9.2×10^{17} m^{-3} (Fig. 1b and Supplementary Fig. 2). To improve the thermal stability, slow-diffusing Sc (0.3 wt.%) was then added into the Al-Cu-Mg-Ag alloy (hereafter denoted as Al-Cu-Mg-Ag-Sc alloy). Under the same initial aging treatment at 185 °C, Ω nanoprecipitates were similarly created in the Sc-added alloy, with number density a little lower while average size somewhat greater than in the Sc-free counterpart (see Supplementary Fig. 3). The addition of Sc did not change the nature of nanoprecipitates; the parameters of the precipitates were only slightly varied by affecting the nucleation thermodynamics and growth kinetics. The nucleation of Ω nanoprecipitates requires the necessary accommodation of Mg and Ag atoms[27]. Since the Sc atoms have a strong binding with both the Mg and Ag atoms [29] and the Sc diffusivity is far slower than the Mg and Ag, the addition of Sc will trap some Mg and Ag atoms and limit their movement. As a result, the nucleation of Ω nanoprecipitates should be negatively affected, leading to a reduction in number density, and consequently an increase of their size once the precipitation of Ω is completed. APT examinations detected only a minor Sc segregation at the Ω/matrix interfaces (Supplementary Fig. 4). Besides, almost no change was found in the interfacial Mg and Ag concentrations between the Al-Cu-Mg-Ag and the Sc-added alloys.

However, when the Al-Cu-Mg-Ag-Sc alloy was exposed to elevated temperatures, the nanoprecipitates exhibited a completely different evolution compared to the Sc-free alloy. After holding at 400 ºC for 10 h, fine coherent platelet precipitates were retained (Fig. 1c) and their thickness has hardly increased (Supplementary Fig. 3). The volume fraction and the number density of the nanoprecipitates were estimated to be ~ 1.8 vol.% and ~ 1.8×10^{20} m^{-3}, respectively. As will be detailed below, a phase transformation happened during the elevated temperature ageing where Ω was replaced by a new phase, that we have named the V phase. APT results revealed that the only difference in composition between Ω and V nanoprecipitates is that Sc atoms are homogeneously distributed within the V phase (Fig.1 d vs e and also Supplementary 5). Fig. 1h compares the coarsening resistance of three plate-like nanoprecipitates in our work, *i.e.* V in Al-Cu-Mg-Ag-Sc, Ω in Al-Cu-Mg-Ag, and θ'-Al_2Cu in the Al-Cu alloy. During 300 ºC exposure, the $\{100\}_\alpha$-oriented θ'-Al_2Cu nanoprecipitates coarsen rapidly, the $\{111\}_\alpha$-oriented Ω exhibit a slower but conspicuous growth. In contrast, the V nanoprecipitates, with a similar $\{111\}_{\alpha\text{-Al}}$ orientation (Supplementary Fig. 6), display a much higher coarsening resistance, with only a slight increase in size even after 120 h at 400 ºC (Supplementary Fig. 7).

To compare the precipitation kinetics at high temperature in the Al-Cu-Mg-Ag alloys with and without Sc addition, both initially in an aged condition (with Ω phase), we used *in-situ* monitoring by small angle X-ray scattering (SAXS) at a synchrotron beamline (see details in Methods). This methodology is particularly suited to quantitatively determine the size evolution of nanoprecipitates[30,31]. The heating mode was ramp-type heating from room temperature to 500 ºC, with a heating rate of 20 ºC/min. Monte Carlo analysis of the SAXS signals[30] were performed to extract parameter-free distributions of the characteristic dimensions of the nanoprecipitates during heating (see details in Methods). Figures 1f and 1g present contour plots of the precipitate size distributions (PSDs) in the Sc-free and Sc-added alloys, respectively, upon ramp-type heating. Note that SAXS is more sensitive to the small dimension of the plate-like nanoprecipitates, which means

that it cannot be directly compared to the radius derived from TEM examinations. In the Sc-free alloy, the Ω coarsen remarkably as the temperature raises above ~ 300 ºC (Fig. 1f). At ~ 400 ºC, the nanoprecipitates grow to large size, possibly transformed into equilibrium θ-Al_2Cu phase, and nanoprecipitates of radius smaller than 10 nm totally disappear. In contrast, in the Sc-added alloy, although there is a decrease of the PSD height due to a partial dissolution of precipitates initially present, a constant main size below 10 nm is retained until ~ 400 ºC, and small-sized nanoprecipitates are still detected up to ~ 500 °C (Fig. 1g, see PSDs in supplementary Fig. 8). These findings further prove that the nanoprecipitates are much more stable when Sc is added to the Al-Mg-Cu-Ag alloy, in good agreement with the *ex-situ* TEM results. From the SAXS results, it is of special interest to note that the phase transformation from Ω to V, as will be revealed by TEM further below, is not accompanied by an apparent change or jump in particle size, suggesting a strong interplay between the Ω and V nanoprecipitates.

The highly stable V nanoprecipitates have the potential to yield superior mechanical properties at elevated temperature. Figure 2a shows stress-strain curves of the three alloys mentioned above as well as an Al-Sc alloy (see Methods) tensile-tested at 400 ºC. The Al-Cu-Mg-Ag-Sc alloy displays a tensile strength reaching ~100 MPa, much higher than the other three alloys (all below ~ 40 MPa). The reason is that the V nanoprecipitates are thermally stable and simultaneously in a large volume fraction, while the other three nanoprecipitates are insufficient either in thermal stability (Ω in Al-Cu-Mg-Ag alloy and θ'-Al_2Cu in Al-Cu alloy) or in volume fraction (Al_3Sc in Al-Sc alloy), see Supplementary Fig. 9. Of special interest to note is that our Al-Cu-Mg-Ag-Sc alloy exhibits not only a 400 °C-tested tensile strength twice that of all the commercial Al alloys that could be collected in the literature and databases, but also a room-temperature (RT) yield strength (~ 400 MPa) located in the high-level regime of the commercial Al alloys, see the comparison in insert in Fig. 2 (a) and Supplementary Fig. 10. Evolution of hardness with aging time at 400 ºC is plotted in Supplementary Fig. 11 to further compare the

thermal resistance between the Al-Cu-Mg-Ag-Sc and Al-Cu-Mg-Ag alloys that had been firstly aged at 185 ºC. It is inferred from the hardness evolution that the V phase can be quickly produced (within about 0.5-1.0 h) in the Al-Cu-Mg-Ag-Sc alloy and then remains stable even up to 200 h of exposure (corresponding to the hardness plateau of ~ 88 HV). On the contrary, the Ω phase in the Sc-free Al-Cu-Mg-Ag alloy is quickly transformed into equilibrium θ-Al_2Cu phase at the high temperature of 400 ºC, resulting in a similar hardness plateau but with a value (~ 53 HV) reduced by about 40 % compared to that in the Sc-added alloy derived from the V nanoprecipitates.

Creep tests on the Al-Cu-Mg-Ag-Sc alloy were also performed at 400 ºC within a wide stress range from 20 to 50 MPa (see Methods). Figure 2b shows the steady-state creep rate ($\dot{\varepsilon}$) as a function of applied stress. Compared with some previously reported Al-based alloys or composites[32-35] that have relatively high creep resistance, the present Sc-added alloy sustains steady-state creep rates generally several orders of magnitude slower. Compared to alloys recently developed by additive manufacturing for high temperature applications, such as Al-Ce-Ni-Mn alloys [35], the present alloy strengthened by V nanoprecipitates also presents a higher creep resistance at 400 °C. It can endure a high value of applied stress of ~50 MPa with $\dot{\varepsilon}$ below 10^{-6} s^{-1}, which marks a major step for Al alloys to be serviced at 400 ºC.

In-situ phase transformation via interstitially-ordered Sc uptake

TEM analysis (Supplementary Fig. 6) determines that the V nanoprecipitates are oriented according to coherent relationships $[001]_v \parallel [211]_\alpha$, $[010]_v \parallel [110]_\alpha$, and $[100]_v \parallel [111]_\alpha$, similar to the Ω phase[26]. To demonstrate a possible strong correlation between the V and Ω nanoprecipitates, controlled experiments were performed. As ~ 460 ºC is the dissolution temperature of Ω phase [26], Ω nanoprecipitates will be fully absent beyond this temperature. We heated the as-solutionized Al-Cu-Mg-Ag-Sc alloy directly at 480 ºC for an hour, and detected no V nanoprecipitates by careful TEM examinations. On the contrary, the V nanoprecipitates were rapidly formed within 15 min at

480 ºC in the same alloy containing initially Ω precipitates (formed during a first aging treatment). One can infer that the Ω phase is a precursor for the V phase nucleation.

APT results (Supplementary Fig. 5) indicate that the V phase contains Sc atoms. Quantitative analysis showed that the introduction of Sc atoms did not change the stoichiometry of Al and Cu, and the V phase has a chemical composition of Al:Cu:Sc ≈ 8:4:1. We next compared the atomic structures of the two phases by high-angle annular dark-field scanning transmission electron microscopy (HAADF-STEM). Figures 3a and 3d show representative aberration-corrected HAADF-STEM images of the Ω phase with the incident electron beam aligned along the $[100]_{\Omega}$ and $[010]_{\Omega}$, respectively, with corresponding fast Fourier transform (FFT) pattern and structure model inserted. The Ω phase has an orthorhombic unit cell with a = 4.96, b = 8.56, and c = 8.48 Å, and a nominal composition of Al_2Cu. Similarly, representative images of the V phase are shown in Figs. 3b and 3e, respectively. The V phase has fundamentally the same structure skeleton as the Ω phase. In addition, in the FFT images, additional sets of patterns indicative of substructure are clearly detected (marked by yellow arrows), in addition to the strong fundamental patterns. The substructure visualized from the FFT images assumes to be the signature of a periodical locally ordered structure.

After examining the aberration-corrected HAADF-STEM images carefully, we found that the Sc atoms are not in substitutional position within the new structure, by partially replacing Al or Cu atoms. Instead, the Sc atoms regularly occupy interstitial positions of the orthorhombic Al-Cu atomic structure. Viewed along the $[001]_V$ direction, the interstitial Sc atoms are alternatively present, forming a high-order symmetric structure. The interstitial Sc occupancy leads to an atomic-scale superstructure in the V phase. We further carried out energy-dispersive X-ray spectroscopy (EDS) mapping with atomic resolution. Figures 3c and 3f show EDS maps of the V phase along $[001]_V$ and $[010]_V$ direction, respectively. In both cases, the interstitial Sc occupancy is visible, which distinguishes the V phase from Ω phase. Simply superposing the atomic structure of Ω phase

with the interstitial Sc, the simulated HAADF and FFT images were fully consistent with the experimental ones (Supplementary Figs.12 and 13). This atomic arrangement has been further confirmed by XRD patterns which show diffraction peaks compatible with the proposed structure (see Supplementary Fig. 15). The high similarity in atomic structure between the V and Ω phases points towards an in-situ phase transformation from Ω to V, which could rationalize the SAXS results of no apparent change in precipitate size during the phase transformation (Fig. 1g).

Atomic structure of the Ω and V phases are illustrated in Fig. 3g and 3h, respectively, and the structural evolution is schematically shown in Supplementary Fig.14. Unlike small-sized atoms which are generally found in interstitial position, the size of Sc atoms is larger than that of both Al and Cu. Periodical Sc occupancy in interstitial positions thus requires regular displacement of some Al and/or Cu atoms. Structural analysis indicated that all of the Al atoms experienced a displacement, while the Cu atoms maintained their positions unchanged. Somewhat similar to pillarlike Si columns-mediated precipitate evolution in Al-Mg-Si alloys[36], the Cu frame serves as a skeleton to coordinate the Ω-to-V transformation. The interstitially Sc-occupied V phase has an atomic bonding stronger than both the Ω and the θ'-Al_2Cu phases, as evaluated from DFT simulations of formation energy per atom (Fig. 3i), see Method. This indicates that the V phase should be more thermally stable than the latter two phases.

The HAADF and APT examinations captured different stages of the Ω to V transformation (Figs. 4a-c). In the Al-Cu-Mg-Ag-Sc alloy exposed to 400 ºC for 10 min, all the nanoprecipitates are Ω phase with interfacial Mg/Ag segregation (Fig. 4a). A small amount of Sc atoms segregated at the interfaces was also detected, although most Sc atoms were dissolved in the Al matrix. After being exposed to 400 ºC for 30 min, some Sc atoms have entered the Ω nanoprecipitate and organized into interstitial ordering. Parts of the Ω phase are locally transformed into V phase (Fig. 4b). Nanoprecipitates fully consisting of the V phase were observed after holding for 4 h at 400 ºC

(Fig. 4c), indicative of a completed phase transformation. The intermediate state as shown in Fig. 4b soundly proves an in-situ phase transformation from Ω to V.

At this point, the present V phase can clearly be distinguished from the so-called W phase that is frequently observed in Al-Cu-Sc alloys, especially with a high Cu content. It has been claimed that the formation of W phase is closely associated with the large-sized equilibrium θ phase[37], since two possible formation mechanisms have been proposed[38]. However, the details of W phase formation at the atomic scale are still unclear and the crystal structure of W phase is not fully determined. Furthermore, the composition of W is $Al_{8-x}Cu_{4+x}Sc$ ($0 < x < 2.6$) [38], showing a variety in composition. In comparison, the V phase is transformed from the nanosized Ω phase, having a constant composition of Al_8Cu_4Sc and maintaining a nanometer size. Another significant difference lies in that the V phase is coherent with the Al matrix, with a habit plane of $(111)_\alpha$, while the W phase has no fixed orientation relationship with the matrix and is completely incoherent with the matrix. Although they are close in composition, the V phase is different from the W phase in almost all aspects including size, morphology, distribution, and phase transformation mechanism.

Sc diffusion aided by coherent ledge

Interstitially-ordered solute occupancy in the present phase transformation shows two characteristics. The first is that large-sized Sc atoms rather than small-sized atoms (such as C, N, O) occupy the interstitial positions. The other is that the interstitially-ordered Sc occupancy is dominated by solute diffusion, rather than a collective behavior. Assembling of both high-solubility Cu and slow-diffusing Sc atoms into the coherent V nanoprecipitates is accomplished through the in-situ Ω-to-V phase transformation, which is controlled by Sc diffusion. Sc diffusion must include two stages, that is, transfer from the solid solution to the Ω phase and diffusion within the Ω phase. Considering that the Mg-Ag segregation layer at the interfaces could prevent the Sc atoms from crossing the interface, Sc diffusion into Ω phase is believed to play a pivotal role in controlling the

V formation. Below, we will focus on the underlying mechanism that is responsible for the Sc entrance into Ω phase.

After comprehensively analyzing the HAADF results on uncompleted Ω-to-V transformation, we observed that the V phase formation begins where a ledge is present on the interface (typically marked by an arrow in Fig. 4b). Figure 4d shows multiple V phase being formed in a single Ω nanoprecipitate (named V-1, V-2, and V-3), all corresponding to ledges present at the Ω-interface (more figures in Supplementary Fig. 16). Differential scanning calorimetry (DSC) results (see Method and Supplementary Fig. 17) determined a critical temperature of ~ 300ºC for V phase formation. The number of visible ledges on Ω plates were experimentally found to increase above 300 ºC[27]. This coincidence additionally demonstrates a strong correlation between the V phase and the ledges. Although ledge migration is generally recognized as the growth mechanism of plate-like nanoprecipitates[39,40], the ledge opens another function in the present phase transformation, which is to trigger Sc diffusion by providing a specific diffusion channel. According to previous experimental findings[27], Mg-Ag segregation layer at the interfaces of Ω nanoprecipitates is broken down at the migrating ledge. The segregation layer was shown to exist at the terraces of migrating ledges, while deficient at the riser of the ledges[27]. This was interpreted as a lack of Ag segregation to the riser[41], supported by the present elemental mapping results (Supplementary Fig. 18). Accompanying the ledge migration, necessary Mg and Ag redistribution (from the original broad interface to the terrace of the migrating ledge) and Cu flux (from the matrix to the riser of the migrating ledge) are mixed in the local region. The Mg-Ag segregation layer integration is destroyed at corner and riser of the migrating ledge, offering a chance for Sc intrusion into Ω.

The orientation relationship between Ω and the matrix aligns the precipitate *c* lattice parameter (with a length of 8.48 Å[38]) with the [111] direction in the matrix (having an interplanar spacing of 2.338 Å). Therefore, there is a large negative strain of ~9.3% normal to the face of the

Ω plate. Two types of ledges have been observed in previous reports[27,43] and also in the present work (as representatively shown in Fig. 4d). The first are small coherent ledges (CLs) and the others are larger ledges containing a misfit-compensating dislocation (ML). The CLs are small ledges which are usually associated with a slight thickening of the Ω plate towards the plate center. Quantitatively, the CLs have a height of about 4.5 Å that matches the height of two $(111)_\alpha$ planes with one-half the Ω unit cell. Since $\frac{1}{2}[001]_\Omega = 4.24$ Å and $\frac{2}{3}[111]_\alpha = 4.676$ Å, each CL produces an additional negative strain of ~9.0% to the pre-existing strain field normal to the Ω plate. This misfit strain is accordingly considered large, which produces a vacancy-type strain field (or tensile strain filed) normal to the broad face adjacent to the CLs[27]. This strain field can be experimentally visualized by geometrical phase analysis (GPA) based on a representative HAADF image of a CL (Supplementary Fig. 19a), see Supplementary Fig. 19b. The large strain field associated with each CL affects their relative spacing by repelling adjacent CLs, thus limiting the density of CLs on the Ω plate. Since the CLs are coherent with the matrix, there are no other mechanisms that may be operating to reduce the misfit, except for local elastic relaxation. The Sc atoms prefer to segregate at CLs and provide continuous Sc supply for the Ω-to-V transformation. In contrast, MLs are large ledges containing a compensating misfit dislocation which accommodates the difference in planar spacing between the two phases[42]. MLs are much less common than CLs, usually concentrated near the plate edges[42]. An interstitial-type strain field (or compressive strain field, see Supplementary Figs. 19d-f) is produced normal to the broad face adjacent to the MLs, which makes it difficult to attract Sc atoms gathered at the MLs. In fact, our abundant HAADF results provide sound evidence that only the CLs aided the V formation while the MLs did not. As the CLs are predominant over the MLs in density, the V formation is substantially homogeneous within the material.

Our observations commonly found that several V nanoprecipitates lie in a straight line in the edge view (Fig. 4e). These interrupted V phase segments result from a competition between the V formation and the Ω dissolution. The Ω phase gradually dissolves at the high temperature of 400

ºC. However, the V formation in-situ from Ω relies on diffusion-controlled interstitial Sc occupancy. The two opposite processes wrestle upon a time dependence and upon Sc availability in solid solution. Where the Sc diffusion and interstitial occupancy results in the V phase the precipitates survive, while the regions remaining as Ω phase dissolve. Consequently, the Ω nanoprecipitates with a large initial diameter finally split into several V plates. Because V nanoprecipitates are template-nucleated and grown on Ω nanoprecipitates, they reach a large volume fraction that is impossible to achieve by Al-Sc binary nanoprecipitates. Qualitatively, 3 Al atoms are bonded with 1 Sc atom to constitute coherent Al_3Sc phase. The present V phase, with a nominal composition of Al_8Cu_4Sc (Supplementary Fig. 5), needs 12 (Al+Cu) atoms to match a Sc atom. Assuming that all added Sc atoms are consumed to form nanoprecipitates, V nanoprecipitates should have a volume fraction several times that of Al_3Sc ones. The high thermal stability of V phase, much surpassing the Ω as revealed in Fig. 4e, is related to the participation of slow-diffusing Sc atoms. First, the Sc substructure interspersed with main Al-Cu structure intensifies the atomic bonding in the V phase and hence suppresses the dissolution at elevated temperatures. Second, Sc has quite limited solubility and slow diffusivity in the Al matrix, which limits Ostwald ripening among V nanoprecipitates. Supplementary Fig. 20 shows calculation results on the atomic structure evolution and corresponding energy variation of a Ω unit cell after Sc atoms infiltrated interstitially. These calculations demonstrate that the regular movements of Al atoms, leading to the same final crystal structure as experimentally observed, reduce the system energy to a stable plateau.

Recent reports revealed that reducing interfacial energy is an effective approach to stabilize nanoprecipitates [44,45] and decreasing PFZs (precipitate-free zones) content is capable of improving the creep resistance of Al alloys [46]. These influencing factors were also examined in this work to understand their contributions. The interstitial Sc occupancy in the V phase does not change the atomic structure of the coherent broad interface, which means the V phase has the same broad interface as its Ω precursor phase with two atomic layers of Mg and Ag segregation unaltered (see

Supplementary Fig. 6). The difference in broad interface energy between the Ω and V phases must be therefore very small. Concerning the semi-coherent peripheral interface free of Mg-Ag segregation (see Supplementary Fig. 21), DFT simulations present a quantitative comparison that the interfacial energy (~ 535.3 mJ/m^2) of V phase, which is only slightly lower than that (~ 549.1 mJ/m^2) of the Ω one (see Supplementary Fig. 21). This indicates that the Sc-induced change in crystal structure truly causes a reduction in the peripheral interface energy and makes a contribution to precipitate stabilization, but the interfacial energy effect is not the predominant one responsible for the great improvement in creep resistance found in the Al-Cu-Mg-Ag-Sc alloy. Similarly, the PFZ effect could be also excluded as the predominant one. The grains have a large size up to 2-3 mm and the width of V-related PFZs is ~ 0.5 μm in the Al-Cu-Mg-Ag-Sc alloy (see Supplementary Fig. 22), indicative of a small PFZ fraction that is the prerequisite for high creep resistance [46]. However, the Sc-free Al-Cu-Mg-Ag alloy, containing grains and Ω-related PFZs with sizes comparable with those of its Sc-added counterpart, displayed high-temperature mechanical properties much inferior to those of the Sc-added alloy. This further demonstrates that the intrinsic stability of the V nanoprecipitates is the key factor guaranteeing the unprecedent creep resistance even at 400 ºC.

In addition to the ramp-type heating results from DSC and SAXS, we further explored a rough temperature window for the isothermal Ω-to-V in-situ phase transformation. Exposing the 185 °C-aged Al-Cu-Mg-Ag-Sc alloy to 250 °C, no V phase was detected until the Ω nanoprecipitates were completely transformed into equilibrium θ-Al_2Cu ones. When the exposure temperature to 300 °C, the V nanoprecipitates were clearly found, but in a relatively low volume fraction. Only about a quarter of the particles were V nanoprecipitates after holding for 50 h, and the others were coarse θ-Al_2Cu particles (see Supplementary Fig. 23). At 350 °C for 50 h, more Ω nanoprecipitates were transformed into V, and the V percentage (f_V/f_T : the ratio of V-nanoprecipitate volume fraction to the total volume fraction of all the precipitates) raised to ~ 70 %. Finally at 400 °

C, full V nanoprecipitates were observed after 2h-holding, free of θ-Al_2Cu particles. The size, number density, and volume fraction of V nanoprecipitates remained almost unchanged up to 120 h at 400 ° C, indicative of an extremely high thermal stability. The isothermal results, basically consistent with the DSC and SAXS results, manifest the controlling factor of temperature in the Ω-to-V in-situ phase transformation, mainly due to thermally-driven Sc diffusion and coherent ledge formation.

A scenario of the in-situ phase transformation from Ω to V can be summarized as follows (see the corresponding sketch in Fig. 4f): at temperature above 300 ºC, coherent ledges are present on the interfaces of Ω nanoprecipitates, together with a large strain field around Ω. Sc atoms are gathered at riser along the ledges, diffusing into the Ω and transforming it gradually to the V phase (Supplementary Fig. 24). The regions that the Sc atoms have not reached are dissolved, in competition with the V growth and with the limited availability of Sc. Finally, nanoprecipitates consisting of fully V phase remain. The V nanoprecipitates derived from a single Ω precipitate lie in the same straight line, as experimentally observed at the edge (Fig. 4e). In the whole process, coherent ledges with interrupted Mg-Ag segregation layer are the key factor that aids the assembling of slow-diffusing Sc and high-solubility Cu solutes into highly-stable coherent V nanoprecipitates.

Interestingly, the Ω-to-V phase transformation proceeds by Sc diffusion within the Ω nanoprecipitates preferentially along the thickness, *i.e.* normal to the broad interfaces, rather than equivalently in all directions (see Fig. 4b and Supplementary Fig. 16). This preferential diffusion can be explained in the following way: (i) Energy-minimizing requirement of this in-situ phase transformation. Interface energy is a key factor in the energy minimization, as well demonstrated in coherent precipitation in the Al alloys [45]. Interfaces between Ω and V are created during the phase transformation, and minimized interfaces are energetically favorable in the course of V nucleation/growth. As the parent Ω precipitates have a high aspect ratio, the diameter is much

greater than the thickness. Accordingly, the V/Ω interface area is much smaller when the V phase grows preferentially along the vertical direction (thickness direction) than radially on the parallel plane (parallel to the broad face). (ii) Stress-accommodation requirement: stress/strain also plays an important role in the transformation. As seen Supplementary Fig. 19, the coherent growth ledge with vacancy-type strain fields causes local tensile stress vertically on the Ω precipitate[27]. Simulations have shown[47,48] that tensile stresses increase the diffusion coefficient of interstitial atoms while it is reduced by compressive stresses.

Another question raised by this Ω-to-V phase transformation is why a similar phase transformation via interstitially-ordered Sc occupancy does not happen within the θ′ nanoprecipitates in the Al-Cu-Sc alloys[21]. From our present results, we can conclude that both spatial and temporal requirements should be simultaneously met to enable the Ω-to-V transformation. Concerning the spatial requirement, interstitial sites with sufficient size should exist in the precursor precipitates for the subsequent Sc residence. Concerning the temporal requirement, the Sc atoms should quickly infiltrate into the precursor precipitates and occupy the regular interstitial sites to form the more stable new phase before the precursor precipitates coarsen and transform into large-sized equilibrium phase. In this case, a fast diffusion-channel is needed for the Sc infiltration while the precursor precipitates should keep thermal stability for a period even at elevated temperatures. As for the spatial requirement, there are double-hexagonal pyramid interstitial sites existing regularly within the Ω precipitates (See the crystal structure model in Supplementary Fig. 25), but similar interstitial sites are not found within the θ' ones. The size of interstitial sites is also large enough in the Ω precipitates, which will be make the atom interstitial occupancy possible. As for the temporal requirement, formation of coherent growth ledges at the broad face of Ω precipitates is highly promoted at temperature greater than ~250 °C[27], despite of the interfacial Mg-Ag segregation layer still remaining. The coherent growth ledges provide fast diffusion-channels for the Sc infiltration. At the same time, the growth ledges are strongly pinned

by the continuous Sc atom flux and other regions are stabilized by the interfacial Mg-Ag segregation layer, which ensures enough time for the Sc diffusion and interstitial occupying within the Ω precipitates. In the Al-Cu-Sc alloy, however, Sc atoms are prone to segregate at the broad face of θ' precipitates to reduce interfacial energy. The interfacial Sc segregation layer is so integral that no coherent growth ledges could be detected at the broad face even exposed to 300 °C for a long time [49] (also see Supplementary Fig. 26a). The absence of coherent growth ledges means no fast diffusion-channels for the Sc filtration. If the temperature is further increased to above 350 °C, the interfacial Sc segregation will transform locally into Al_3Sc precipitates, and the Sc covering-free regions of θ' precipitate will quickly dissolve or fast coarsen to equilibrium θ phase (see Supplementary Fig. 26b), making no chances for the phase transformation to V.

We end by illustrating that the interstitial solute stabilizing strategy described in this article will be equally effective for producing other stable nanoprecipitates in Al-Cu-Mg-Ag alloys. Our further experimental results show that the addition of slow-diffusing Zr, Mn or Ce, instead of Sc, into the Al-Cu-Mg-Ag alloys could produce highly-stable nanoprecipitates. These nanoprecipitates have a high content of Zr (or Mn, Ce) atoms inside (Supplementary Fig. 27), indicative of a possible formation mechanism similar to Sc-driven V formation. The key ingredient for the strategy in this work is an in-situ phase transformation aided by coherent ledges, which couples slow-diffusing solutes with high-solubility solutes into coherent nanoprecipitates. A spatially and time-resolved investigation of the templated phase transformation, at the atomic length scale, enables a deeper understanding, and hence an unusual control of the coarsening-resistant nanoprecipitates to achieve an unprecedent high-temperature stability and creep resistance in light-weight Al alloys. Since coherent plate-like precipitates similarly with ledges as growth mechanism are widely found in various alloys, such as Mg alloys[50], Ni alloys[51], Cu alloys[52], Ti alloys[53], and steels[54], we anticipate that the ledge-mediated interactions between different solutes should be also applied in these alloys to excite unexpected phase transformation upon nanoprecipitates for improved performances.

Methods

Materials fabrication. Alloys with composition of Al-4.5 wt.%Cu, Al-0.3 wt.%Sc, Al-4.5 wt.%Cu-0.3 wt.%Mg-0.4 wt.%Ag and Al-4.5 wt.%Cu-0.3 wt.%Mg-0.4 wt.%Ag-0.3 wt.% Sc were respectively melted and cast in a stream argon, by using 99.99 wt.% pure Al, 99.99 wt.% pure Cu, 99.99 wt.% pure Mg, 99.99 wt.% pure Ag, and master Al-2.0 wt.% Sc alloy. For each alloy, 10 kg-weighted raw materials with designed composition were melted in an alumina crucible at 750 °C, stirred three times to fully mix the alloying elements, and then poured into a steel mold with a gating system that was pre-heated at 200 °C. Cylindrical samples with 120 mm in diameter and about 1500 mm in length were produced after air cooling. Specimens of Φ12mm in size were cut from the ingots and subjected to further heat treatments. Table 1 summarizes the heat treatments of the alloys used in this study. Note that the additional solution treatment at 560 °C was made in order to avoid overburnt, but guaranteeing enough Sc atoms for the subsequent Ω-to-V phase transformation.

Table 1 Summary of the heat treatments of the alloys

Alloy	Homogenization treatment	Solution treatment	Aging treatment
Al-Sc	460 ºC /3 h	510 ºC /12 h-560 ºC /9 h	300 ºC /9 h
Al-Cu	460 ºC /3 h	510 ºC /12 h-560 ºC /9 h	185 ºC /4 h
Al-Cu-Mg-Ag	460 ºC /3 h	510 ºC /12 h-560 ºC /9 h	185 ºC /4 h
Al-Cu-Mg-Ag-Sc	460 ºC /3 h	510 ºC /12 h-560 ºC /9 h	185 ºC /4 h

Microstructural characterization. To study the microstructures at nanoscale, high-angle annular dark field (HAADF) scanning transmission electron microscopy (STEM) and energy-diapersive X-ray analysis (EDX, Bruke Super-X, Bruke, USA) were performed using Cs-STEM (FEI cubed Themis, Thermo Fisher Scientific Inc, USA) operating at 300kV. TEM foils were prepared by following standard electro-polishing techniques for Al alloys. Samples for TEM observation were sliced into 0.3 mm thick pieces using a slow speed saw, punched into 3 mm diameter discs and ground to ~150 μm thickness. Electropolishing was conducted using Struers Tenupol-5 twin-jet electropolishing machine with a 30% nitic acid solution in methanol at -30 °C and 15 V. The diameter and thickness of each particle were measured within the TEM micrographs with the electron beam oriented parallel to the $[110]_\alpha$ zone axis for Ω and V precipitates and $[100]_\alpha$ zone axis for θ'-Al_2Cu and Al_3Sc. For Ω and V precipitates. The number density of plate-like precipitate per

unit volume of the matrix phase, N_V, can be evaluated using the following equation[55]:

$$N_V = \frac{N+N\left((t+d)/\sqrt{A_S}\right)}{A_S(t+d)} \quad (1)$$

where N is the number of counted particles on the TEM images, A_S is a respective area on the TEM image, t is the thickness of the foil area and d is the measured mean diameter. The number density per unit volume of the matrix phase(N_V) of the plate-like θ'-Al_2Cu precipitates can be expressed as[56]:

$$N_V = \frac{N+N\left((t+d)/2\sqrt{A_S}\right)}{A_S(t+d)} , \quad (2)$$

The volume fraction of plate-like precipitates is estimated using the following equation:

$$f = \frac{N_V \pi d^2 t}{4} , \quad (3)$$

The number density of spherical precipitates (*e.g.*, Al_3Sc precipitates), N_V, is determined using the equation as below[21]:

$$N_V = \frac{N}{(t+d)}, \quad (4)$$

where N is a number of counted particles on the TEM images, t is the thickness of the foil area and d is the measured mean diameter. And the volume fraction is estimated as:

$$f = \frac{4N_V \pi d^3}{3}. \quad (5)$$

APT experiments were performed using a Local Electrode Atom Probe (LEAP 4000HR) from CAMECA. Specimens for APT were prepared by wire-cutting small blanks ($0.3 \times 0.3 \times 10$ mm^3) using a combination of slicing and mechanical grinding. A two-step electropolishing procedure was subsequently employed for APT tips preparation, a 10 vol% perchloric acid in methanol solution was used for rough polishing, and the final polishing was performed using a solution of 2 vol% perchloric acid in butoxyethanol. APT data collection was performed at a specimen temperature of 30 ± 0.3 K, a voltage pulse fraction (pulse voltage/steady-state direct current voltage) of 19 %, a pulse frequency of 200 kHz, and a background gauge pressure of < 6.7 x 10^{-8} Pa (5 x 10^{-10} torr). Tomographic reconstruction and analysis of APT data were carried out using IVAS™ 6 software.

SAXS measurements. The SAXS measurements were carried out on the BM02-D2AM beamline of the European Synchrotron Radiation Facility (ESRF). Samples were thinned to a thickness of 0.5 mm before the measurements. The SAXS measurements along the precipitation sequence were carried out at a photon energy of 12 keV, with a sample-to-detector distance of 3.18 m. The SAXS patterns were recorded on a hybrid pixel detector (imXPAD D5). They were subsequently corrected

for the detector flat field, background-subtracted, and normalized to absolute units using the sample transmission as well as a glassy carbon sample as a secondary calibration sample. In-situ experiments were used a 20 K/min heating rate from 25 to 500 °C. The signal was interpreted as originating from a distribution of spherical objects using a custom Monte Carlo size distribution retrieval method[30] to get a view of the evolution of the characteristic dimensions of the precipitates during heating. The actual precipitates are non-spherical and give rise to an anisotropic signal which is strongly dependent on the local texture of the irradiated volume and the orientation of the precipitates. Rather than attempting to account for these complex effects, we have used an isotropic assumption and limited ourselves to a qualitative interpretation of the results.

Measurements of mechanical properties. The tensile tests were performed using an INSTRON 5982 multifunctional mechanical tester. The dogbone-shaped tensile specimens have a gauge dimension of 6 mm × 2 mm × 25 mm. High temperature tensile testing at 400 °C was performed strictly according to the ASTM E21 standard. Vickers hardness measurements were performed with a Wilson VH3300 Vickers Hardness tester (Buehler) using a 200 g load applied for 15 s on samples polished to a 1 μm surface finish. Twenty indentations were made in each specimen across different grains to ensure the reliability of data. Dogbone-shaped creep samples with a gauge size of 5 mm in diameter and 25 mm in length were prepared for creep, and two extra lugs were machined in the creep specimens to mark the gauge section of the creep specimen and clamp the extensometer to measure sample displacement. During the constant load creep test, the specimens were heated to 400 ℃ and hold for 0.5 h, and different creep stresses (25, 30, 40, and 50 MPa) were respectively applied to measure the tensile creep curve and determine the steady-state creep rate as a function of applied creep stress.

Density functional theory (DFT) calculations. All the DFT calculations were carried out by using the projector augmented wave (PAW) potentials implemented in Vienna Ab-initio Simulation Package (VASP)[57,58]. Perdew-Burke-Ernzerhof (PBE) exchange-correlation functional of generalized gradient approximation was used (GGA-PBE)[59]. A plane-wave cut-off of 520 eV was taken for all the calculations. For the crystal structures and interface structures, Monkhorst-Pack meshes with a density of 12 × 12 × 12 and 6 × 6 × 2 were chosen, respectively. The convergence criteria for energy and force are 10-4 eV and 0.05 eV/Å, respectively. The formation energy of a compound per atom was evaluated by using the following equation[60]:

$$\Delta H^{formation}(Al_aCu_bSc_c) = \frac{E(Al_aCu_bSc_c)-[n_{Al}E(Al)+n_{Cu}E(Cu)+n_{Sc}E(Sc)]}{n_{Al}+n_{Cu}+n_{Sc}}, \quad (6)$$

where $E(Al_aCu_bSc_c)$, $E(Al)$, $E(Cu)$ and $E(Sc)$ are DFT-calculated total energies of the

compound $Al_aCu_bSc_c$, constituents pure Al, Cu and Sc in their equilibrium crystal structures, respectively; and n_{Al}, n_{Cu} and n_{Sc} are the number of elemental atoms in the compounds.

The interfacial energy was calculated by following the method proposed by Wolverton[61]. For a supercell containing interface, the supercell formation energy is expressed by the strain and interfacial contributions:

$$\Delta E_f = \delta E_{CS}(Al, V/\Omega) + 2\sigma A/N, \quad (7)$$

where $\delta E_{CS}(Al, V/\Omega)$ is the coherency strain per atom caused by the lattice mismatch between the Al matrix and V (or Ω) nanoprecipitate, *N* is the total number of atoms in the supercell, σ is the interfacial energy, *A* is the interfacial area, and $\Delta E_f = \left[E^{\text{total}}_{(Al,V/\Omega)} - n\mu_{Al} - n\mu_{Cu} - n\mu_{Sc}\right]/N$ is the formation energy per atom relative to the chemical potentials (μ_{Al}, μ_{Cu}, μ_{Sc}) of Al. One can evaluate the interfacial energy by computing the energies of supercells with various sizes and extracting the slope of ΔE_f *vs.* $1/N$ from Eq. (7).

References:

1. Jiang, S., Wang, H., Wu, Y., *et al.* Ultrastrong steel via minimal lattice misfit and high-density nanoprecipitation. *Nature* **544**, 460-464 (2017).
2. Sun, W., Zhu, Y., Marceau, R., *et al.* Precipitation strengthening of aluminum alloys by room-temperature cyclic plasticity. *Science* **363**, 972-975 (2019).
3. Kurnsteiner, P, *et al.* High-strength Damascus steel by additive manufacturing. *Nature* **582**, 515-519 (2020).
4. Yang, Y., *et al.* Bifunctional nanoprecipitates strength and ductilize a medium-entropy alloy. *Nature* **595**, 245-249 (2021).
5. Raabe, D., Tasan, C. C. & Olivetti, E. A. Strategies for improving the sustainability of structural metals. *Nature* **575**, 64-74 (2019).
6. Deschamps, A. & Hutchinson, C. R. Precipitation kinetics in metallic alloys: Experiments and modeling. *Acta Mater.* **220**, 117338 (2021).
7. Hornbogen, E. & Starke, E. A. Theory assisted design of high strength low alloy aluminum. *Acta Metall. Mater.* **41**, 1–16 (1993).
8. Knipling, K. E., Dunand, D. C. & Seidman, D. N. Criteria for developing castable, creep-resistant aluminum-based alloys – A review. *Zeitschrift fuer Metallkunde* **97**, 246–265 (2006).
9. Zhu, A. W., Gable, B. M., Shiflet, G. J., *et al*. The intelligent design of high strength, creep-resistant aluminum alloys. in *Aluminum alloys: Their Physical and Mechanical Properties, Pts*

1-3 & Mater. Sci. Forum **396-4**, 21 (2002).

10. Polmear, I. J. & Couper, M. J. Design and development of an experimental wrought aluminum alloy for use at elevated temperatures. *Metall. Mater. Trans. A* **19**, 1027–1035 (1988).
11. Porter, D. A., Easterling, K. E. & Sherif, M. Y. *Phase Transformations in Metals and Alloys*. (CRC Press, 2021).
12. Zedalis, M. S. & Fine, M. E. Precipitation and Ostwald ripening in dilute Al base-Zr-V alloys. *Metall. Mater. Trans. A* **17A**, 2187–2198 (1986).
13. Marquis, E. A. & Seidman, D. N. Nanoscale structural evolution of Al_3Sc precipitates in Al(Sc) alloys. *Acta Mater.* **49**, 1909–1919 (2001).
14. Clouet, E. *et al.* Complex precipitation pathways in multicomponent alloys. *Nature Materials* **5**, 482–488 (2006).
15. Ryum, N., in Starke, E. A. & Sanders, T. H. (Eds.), *Aluminum Alloys: Their Physical and Mechanical Properties*, Vol. 3, EMAS, Warley, 1511 (1986).
16. Liu, G., *et al.*, Modeling the strengthening response to aging process of heat-treatable aluminum alloys containing plate/disc- or rod/needle-shaped precipitates. *Mater. Sci. Eng. A* **344**, 113-124 (2003).
17. Deschamps, A. & Bréchet, Y. Influence of predeformation and ageing of an Al-Zn-Mg alloy — II. Modeling of precipitation kinetics and yield stress. *Acta Mater.* **47**, 293-305 (1998).
18. Orthacker, A. *et al.* Diffusion-defining atomic-scale spinodal decomposition within nanoprecipitates. *Nature Mater.* **17**, 1101–1107 (2018).
19. Booth-Morrison, C., Dunand, D. C. & Seidman, D. N. Coarsening resistance at 400°C of precipitation-strengthened Al–Zr–Sc–Er alloys.pdf. *Acta Mater.* **59**, 7029–7042 (2011).
20. Polmear, I. J., Nie, J.-F., Qian, M. & StJohn, D. *Light alloys: metallurgy of the light metals*. (Butterworth-Heinemann, an imprint of Elsevier, 2017).
21. Yang, C. et al. The influence of Sc solute partitioning on the microalloying effect and mechanical properties of Al-Cu alloys with minor Sc addition. Acta Mater. 119, 68–79 (2016).
22. Shyam, A. et al. Elevated temperature microstructural stability in cast AlCuMnZr alloys through solute segregation. Mater. Sci. Eng. A 765, 138279 (2019).
23. Kirchheim, R. Reducing grain boundary, dislocation line and vacancy formation energies by solute segregation. I. Theoretical background. Acta Mater. 55, 5129–5138 (2007).
24. Gao, Y. H. et al. Stabilizing nanoprecipitates in Al-Cu alloys for creep resistance at 300°C. Mater. Res. Lett. 7, 18–25 (2019).
25. Michi, R. A. et al. Microstructural evolution and strengthening mechanisms in a heat-treated

additively manufactured Al–Cu–Mn–Zr alloy. Materials Science and Engineering: A 840, 142928 (2022).

26. Muddle, B. C. & Polmear, I. J. The precipitate Ω phase in Al-Cu-Mg-Ag alloys. Acta Metall. 37, 777–789 (1989).
27. Hutchinson, C. R., Fan, X., Pennycook, S. J. & Shiflet, G. J. On the origin of the high coarsening resistance of Ω plates in Al-Cu-Mg-Ag Alloys. Acta Mater. 49, 2827–2841 (2001).
28. Ringer, S. P., Yeung, W., Muddle, B. C. & Polmear, I. J. Precipitate stability in Al-Cu-Mg-Ag alloys aged at high temperatures. Acta Metall. Mater. 42, 1715–1725 (1994).
29. Peng, J., Bahl, S., Shyam, A., Haynes, J. A. & Shin, D. Solute-vacancy clustering in aluminum. Acta Materialia 196, 747–758 (2020).
30. Pauw, B. R., Pedersen, J. S., Tardif, S., Takata, M. & Iversen, B. B. Improvements and considerations for size distribution retrieval from small-angle scattering data by Monte Carlo methods. J. Appl. Cryst. 46, 365–371 (2013).
31. De Geuser, F., Styles, M. J., Hutchinson, C. R. & Deschamps, A. High-throughput in-situ characterization and modeling of precipitation kinetics in compositionally graded alloys. Acta Mater.101, 1–9 (2015).
32. De Luca, A., Seidman, D. N. & Dunand, D. C. Mn and Mo additions to a dilute Al-Zr-Sc-Er-Si-based alloy to improve creep resistance through solid-solution- and precipitation-strengthening. Acta Mater. 194, 60–67 (2020).
33. Ng, D. S. & Dunand, D. C. Aging- and creep-resistance of a cast hypoeutectic Al-6.9Ce-9.3Mg (wt.%) alloy. Mater. Sci. Eng. A 786, 139398 (2020).
34. Wakashima, K., Moriyama, T. & Mori, T. Steady-state creep of a particulate SiC/6061 Al composite. Acta Mater. 48, 891–901 (2000).
35. Michi, R. A. et al. A creep-resistant additively manufactured Al-Ce-Ni-Mn alloy. Acta Materialia 227, 117699 (2022).
36. Chen, J. H., Costan, E., Huis, M. A. van, Xu, Q. & Zandbergen, H. W. Atomic Pillar-Based Nanoprecipitates Strengthen AlMgSi Alloys. Science 312, 416–419 (2006).
37. Toropova, L. S., Eskin, D. G., Kharakterova, M. L. & Dobatkina, T. V. Advanced Aluminum Alloys Containing Scandium: Structure and Properties. (Routledge, 2017).
38. Gazizov, M., Teleshov, V., Zakharov, V. & Kaibyshev, R. Solidification behaviour and the effects of homogenisation on the structure of an Al–Cu–Mg–Ag–Sc alloy. Journal of Alloys and Compounds 509, 9497–9507 (2011).

39. Shiflet, G. J., Aaronson, H. I. & Courtney, T. H. Kinetics of coarsening by the ledge mechanism. Acta Metall. 27, 377–385 (1979).
40. Bréchet, Y. & Purdy, G. A self-consistent treatment of precipitate growth via ledge migration in the presence of interfacial dissipation. Scripta Mater. 52, 7–10 (2005).
41. Reich, L., Murayama, M. & Hono, K. Evolution of Ω phase in an Al–Cu–Mg–Ag alloy—a three-dimensional atom probe study. Acta Mater. 46, 6053–6062 (1998).
42. Knowles, K. M. & Stobbs, W. M. The structure of {111} age-hardening precipitates in Al–Cu–Mg–Ag alloys. Acta Cryst. B 44, 207–227 (1988).
43. Fonda, R. W., Cassada, W. A. & Shiflet, G. J. Accomodation of the misfit strain surrounding {III} precipitates (Ω) in Al-Cu-Mg-(Ag). Acta Metall. Mater. 40, 2539–2546 (1992).
44. Chisholm, M. F. et al. Atomic structures of interfacial solute gateways to θ′ precipitates in Al-Cu alloys. Acta Materialia 212, 116891 (2021).
45. Poplawsky, J. D. et al. The synergistic role of Mn and Zr/Ti in producing θ′/L12 co-precipitates in Al-Cu alloys. Acta Materialia 194, 577–586 (2020).
46. Rakhmonov, J. U., Bahl, S., Shyam, A. & Dunand, D. C. Cavitation-resistant intergranular precipitates enhance creep performance of θ′-strengthened Al-Cu based alloys. Acta Materialia 228, 117788 (2022).
47. Zumpicchiat, G., Pascal, S., Tupin, M. & Berdin-Méric, C. Finite element modelling of the oxidation kinetics of Zircaloy-4 with a controlled metal-oxide interface and the influence of growth stress. Corrosion Science 100, 209–221 (2015).
48. Ziebarth, B., Mrovec, M., Elsässer, C. & Gumbsch, P. Influence of dislocation strain fields on the diffusion of interstitial iron impurities in silicon. Phys. Rev. B 92, 115309 (2015).
49. Gao, Y. H. et al. Segregation-sandwiched stable interface suffocates nanoprecipitate coarsening to elevate creep resistance. Materials Research Letters 8, 446–453 (2020).
50. Zhu, Y. M., et al., Growth and transformation mechanisms of 18R and 14H in Mg-Y-Zn alloys. Acta Mater. 60, 6562–6672 (2012).
51. Chen, G., et al., Effects of ledge density on the morphology and growth kinetics of precipitates in a Ni–Cr Alloy. Acta Mater. 53, 895–906 (2005).
52. Chattopadhyay, K. & Aaronson, H. I. Interfacial structure and crystallographic studies of transformation in β' and β Cu-Zn alloys: I Isothermal formation of α1 plates from β'. Acta Metall. 34, 695-711 (1986).
53. Fu, X. Q., Wang, X. D., Zhao, B. K., et al. Atomic-scale observation of non-classical nucleation-mediated phase transformation in a titanium alloy. Nature Mater. 21, 290-296 (2022)

54. Chai Y. W., Kato, K., Yabu, C., et al. Disconnections and Laves (C14) precipitation in high-Cr ferritic stainless steels. Acta Mater. 198, 230-241 (2020).

55. Gazizov, M. & Kaibyshev, R. Effect of pre-straining on the aging behavior and mechanical properties of an Al–Cu–Mg–Ag alloy. Materials Science and Engineering: A 625, 119–130 (2015).
56. Nie, J. F. & Muddle, B. C. Strengthening of an Al–Cu–Sn alloy by deformation-resistant precipitate plates. Acta Materialia 56, 3490–3501 (2008).
57. Kresse, G. & Hafner, J. Ab initio molecular dynamics for liquid metals. Phys. Rev. B 47, 558–561 (1993).
58. Kresse, G. & Furthmüller, J. Efficient iterative schemes for ab initio total-energy calculations using a plane-wave basis set. Phys. Rev. B 54, 11169–11186 (1996).
59. Perdew, J. P., Burke, K. & Ernzerhof, M. Generalized gradient approximation made simple. Phys. Rev. Lett. 77, 3865–3868 (1996)
60. Kim, K., Zhou, B.-C. & Wolverton, C. First-principles study of crystal structure and stability of T1 precipitates in Al-Li-Cu alloys. Acta Materialia 145, 337–346 (2018).
61. Vaithyanathan, V., Wolverton, C. & Chen, L. Q. Multiscale modeling of θ′ precipitation in Al–Cu binary alloys. Acta Materialia 52, 2973–2987 (2004).

Acknowledgements

This work was supported by the National Natural Science Foundation of China (Grant nos. 51790482 and 52001249) and the 111 Project of China (BP2018008). This work is also supported by the International Joint Laboratory for Micro/Nano Manufacturing and Measurement Technologies. Y.P. acknowledges the support from the National Natural Science Foundation of China (Grant no. 51801087).

Author contributions

G.L., A. D., and J. S. initiated and supervised the project. H. X. and C. Y. prepared the alloys and carried out most of the microscopy and all the mechanical property testing. F. G. did the SAXS experiments and data analysis. H. X., C. Y., P. Z., and J. Z. performed the APT examination and

data analysis. B. C. and Y. P. performed the HAADF examinations. F. L. and J. B. did the DFT calculations. All authors extensively discussed the data. G.L., F. G., A. D., and J. S. wrote the paper.

Competing interests

The authors declare no competing interests.

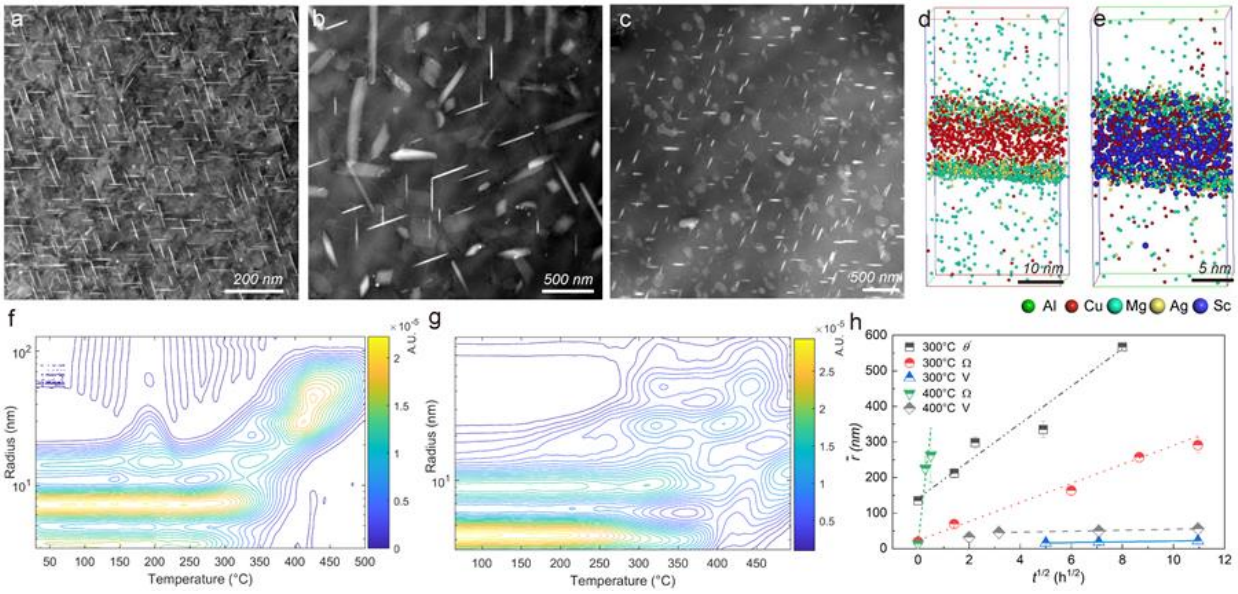

Figure1 Highly stable nanoprecipitates in the Sc-microalloyed alloy. Representative HADDF images to show nanoprecipitates in as-aged Al-Cu-Mg-Ag alloy (**a**) and the alloy exposed to 400 ° C for 0.25 h (**b**), and the Al-Cu-Mg-Ag-Sc alloys exposed to 400 ℃ for 10h (**c**). Representative APT images showing the element distribution within nanoprecipitates in the 400 ℃-exposed Al-Cu-Mg-Ag alloy (**d**) and Al-Cu-Mg-Ag-Sc alloys (**e**). Evolution of the nanoprecipitate radius measured by SAXS in-situ heating from room temperature to 500° C in the Al-Cu-Mg-Ag (**f**) and Al-Cu-Mg-Ag-Sc alloys (**g**). The coarsening behavior of V nanoprecipitates at 300 ° C and 400 ° C, in comparison with the θ'-Al_2Cu in Al-Cu alloy and the Ω in Al-Cu-Mg-Ag alloys (**h**).

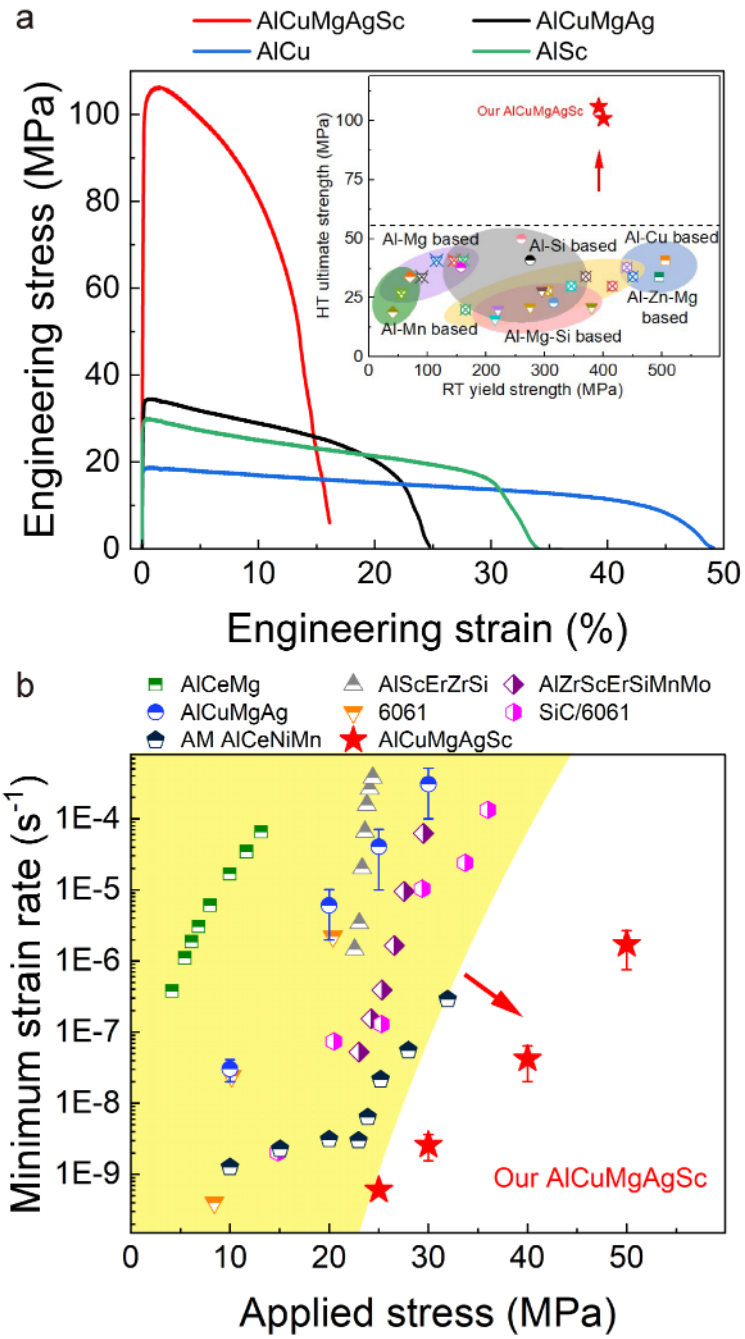

Figure 2 Unprecedent mechanical properties at 400 ° C. (**a**) Engineering stress-strain curves of the Al-Sc, Al-Cu, Al-Cu-Mg-Ag and Al-Cu-Mg-Ag-Sc alloys tensile tested at 400 ° C. Insert shows the 400 ° C-tested tensile strength vs RT yield strength of the present Al-Cu-Mg-Ag-Sc alloy compared with commercial aluminum alloys. (For details see Supplementary Fig.10) (**b**) The applied stress-dependence of steady-state tensile creep rates of present Al-Cu-Mg-Ag-Sc alloy tested at 400 ° C (highlighted by red hexagon), in comparison with previously reported Al-Ce-Mg alloy, Al-Sc-Er-Zr-Si-based alloy, 6061 alloy, SiC/6061 alloy, and AM Al-Ce-Ni-Mn[32-35] tested at 400 °C. Note that the mechanical properties of Al alloys measured at 400 ° C are quite scarce.

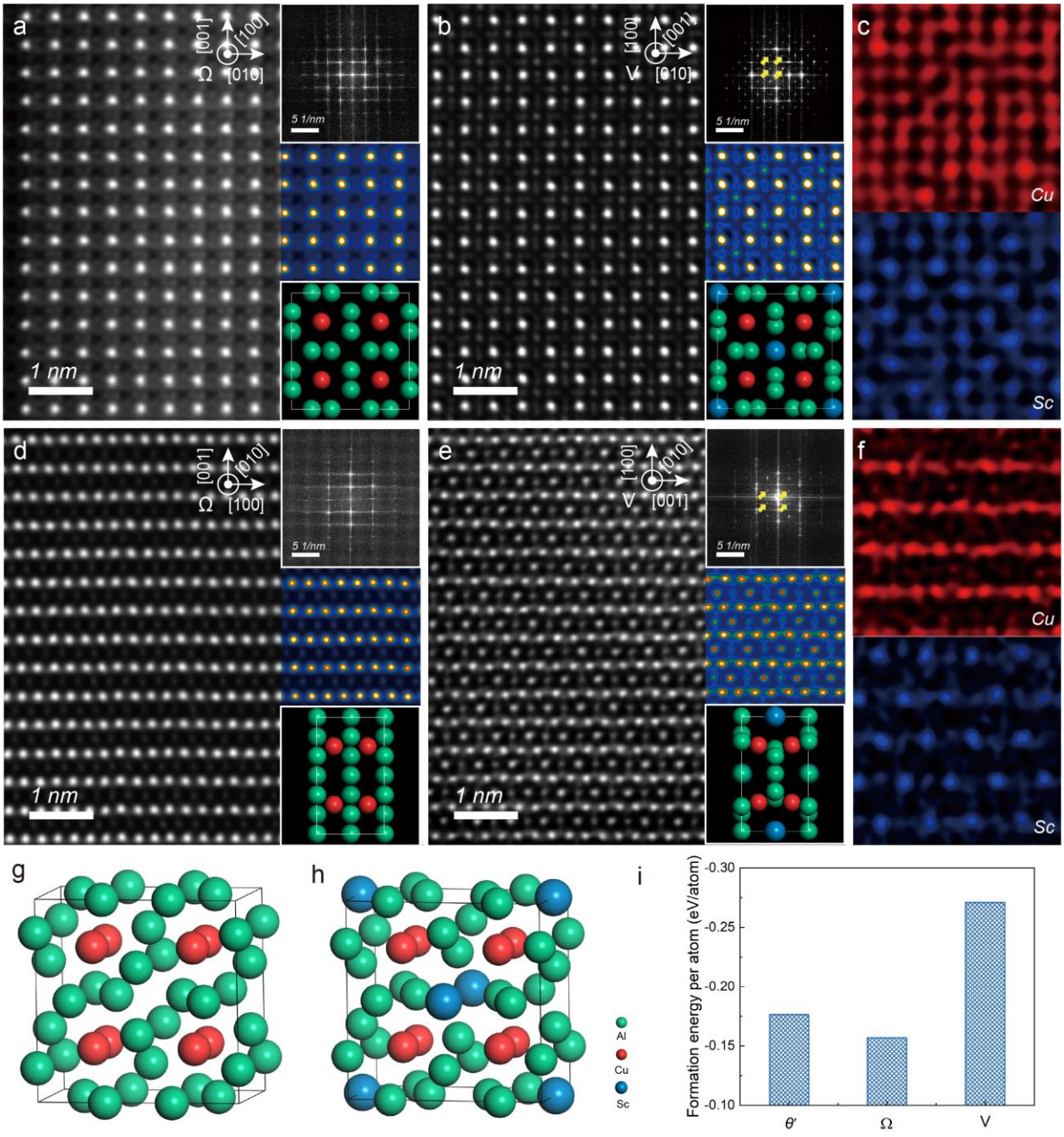

Figure 3 Strong crystal structure with interstitial Sc occupancy. Representative HADDF images, corresponding FFT images (upper-right) and crystal structure (bottom-right) of the Ω nanoprecipitates in Al-Cu-Mg-Ag alloy viewed along $<100>_{\Omega}$ (**a**) and $<010>_{\Omega}$ (**d**), and the V nanoprecipitates in Al-Cu-Mg-Ag-Sc alloy viewed along $<100>_{V}$ (**b**) and $<010>_{V}$ (**e**), respectively. Corresponding elemental atomic mapping showing distribution of Cu and Sc atoms in the V nanoprecipitates viewed along $<100>_{V}$ (**c**) and $<010>_{V}$ (**f**), respectively. Sketches to show the crystal structure of Ω (**g**) and V (**h**) nanoprecipitates, respectively. Interstitial Sc occupancy in the V phase is clear. (**i**) DFT simulation results on the formation energy per atoms of θ', Ω and V precipitates for comparison, where the greater value in minus represents a stronger atomic bonding.

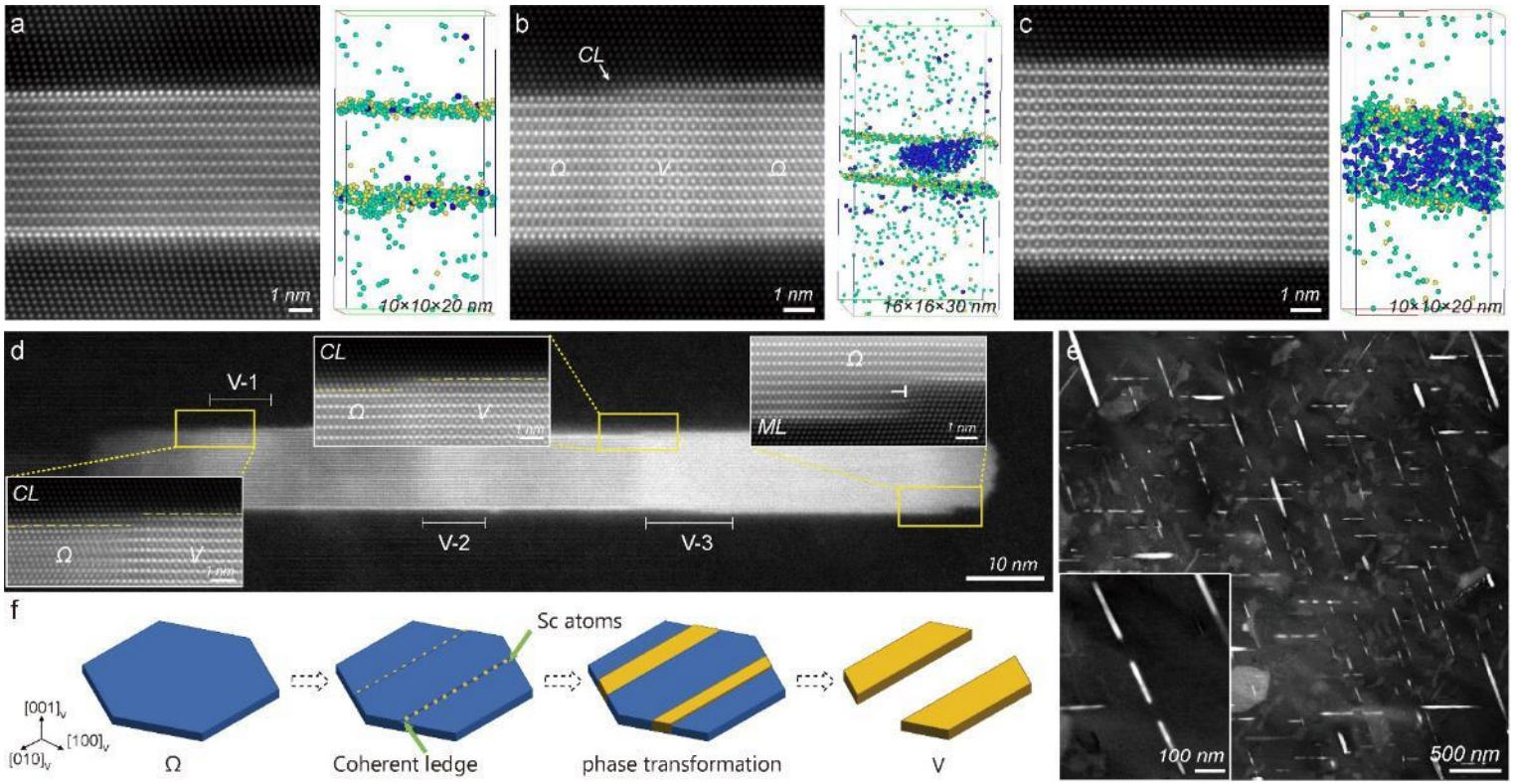

Figure 4 In-situ phase transformation within nanoprecipitates *via* diffusion-dominated interstitial Sc occupancy. Representative HAADF images and corresponding APT images showing different stages of the Ω to V transformation in Al-Cu-Mg-Ag-Sc alloy exposed to 400 ° C (**a**, **b**, and **c**). Nanoprecipitate in full Ω phase is evident at 10 min-holding, with interfacial Mg+Ag segregation (a few Sc segregation) (**a**). A local V phase is in-situ formed at 30 min-holding (**b**). The nanoprecipitate is completely transformed into V phase after 4 h-holding (**c**). Blue, green, and yellow dots represent Sc, Mg, and Ag atoms, respectively. A representative HAADF image showing multiple V phases (named V-1, V-2, and V-3) simultaneously formed within a large Ω nanoprecipitate, all associated with coherent ledges (CLs) (**d**). V phase is not formed at the ML ledge. Inserts are magnified images of the CLs and a ML. A representative TEM image (**e**) shows a common finding that some V nanoprecipitates lie in a straight line on the edge, indicative a splitting during the phase transformation. Insert is a magnified image to illustrate the split nanoprecipitates. (**f**) Sketches to show the CL-aided Sc diffusion into Ω and the in-situ phase transformation from Ω to V, with a competition between V formation and Sc-unreached Ω dissolution.